CHALMERS

_____

CPL

Chalmers Publication Library

Institutional Repository of
Chalmers University of Technology
http://publications.lib.chalmers.se

_____

Flow around a tall finite cylinder explored by large eddy simulation

SINIŠA KRAJNOVIĆ†

Division of Fluid Dynamics, Department of Applied Mechanics, Chalmers University of Technology,
SE-412 96 Göteborg, Sweden

The flow around a finite circular cylinder with a height-to-diameter ratio of 6 was studied using large eddy simulation (LES). The cylinder was mounted on a ground plane where a thin boundary layer with a thickness of only 7 % of the cylinder's diameter was formed. The flow resulting from the present LES was used to present a detailed picture of both the instantaneous and the time-averaged flow. Among the results of the present study is the explanation for the formation of two time-averaged tip vortices from two pairs of instantaneous vortices. The main recirculation region on the cylinder's top was found to be one vortex with both legs attached to the top surface, in agreement with some previous investigations. The mean flow in the near wake region was found to contain two horseshoe vortices, one large arch vortex stretching from the cylinder's top and another vortex resulting from the flow moving down below the rear stagnation point on the cylinder. The instantaneous horseshoe vortex near the ground was found to be unsteady and changed shape over time. The time-averaged flow showed three complete horseshoe vortices, in agreement with previous knowledge. The downwash process above the free end into the near wake occurs at a rather constant angle with respect to the plane normal to the streamwise direction. The same angle was preserved in the inclination of the arch vortex in the time-averaged flow.

Key words: aerodynamics, separated flows, turbulence simulation

1. Introduction

The flow around a cylinder of finite length where one end is mounted on a wall and the other is free is representative of flows in various applications ranging from buildings, gas tanks and chimneys to flame holders in oil refineries and space rockets on launching pads.

One of the earlier studies is by Kawamura *et al.* (1984), which was an experimental investigation of a finite cylinder with an aspect ratio of $L/D = 1$–8 (length/diameter). They reported the existence of a pair of trailing vortices formed from the free end of the cylinder. Furthermore, they found that these trailing vortices together with the downwash flow from the free end into the near wake of the cylinder regulate the Kármán vortex shedding that normally exists behind infinite cylinders. As they nicely sketched in their paper, the existence of the Kármán vortex shedding is directly dependent on the cylinder's aspect ratio and is present only for cylinders for which

---

† Email address for correspondence: sinisa@chalmers.se

the aspect ratio is higher than some critical value. This critical value was later found by different authors to vary between $L/D = 1$ and 7. The reason for the different critical aspect ratio values was found in the influence of the plane boundary layer (Luo 1993).

Another study was conducted by Okamoto & Yagita (1973), who measured the surface pressure coefficients for cylinders of aspect ratios 1–15 immersed in a uniform flow and a Reynolds number of $Re = 1.3 \times 10^4$. The influence of the free end on the near wake flow was found to be limited in their study to the three diameters from the top of the cylinder.

Okamoto & Sunabashiri (1992) studied the influence of the cylinder's aspect ratio on the character of the flow structures in the near wake region at $Re = 2.5 \times 10^4$ and 4.7×10^4. They found that the flow changes above an aspect ratio of 4, with vortex shedding changing from a symmetric arch type to an antisymmetric Kármán type. Their study concentrated on the flow regions in the lower parts of the cylinder, and the influence of the free end was not discussed.

Luo, Gan & Chew (1996) experimentally investigated flows past both one and two in tandem finite length circular cylinders at $Re = 3.33 \times 10^4$. Cylinders with three aspect ratios, 4, 6 and 8, were investigated. One conclusion drawn in their study was the strong influence of the free end flow on the flow that separates along the cylinder. They found that the free end flow delays the separation of the flow along the cylinder, resulting in a less negative wake pressure and lower drag when compared with the drag of the infinite cylinder.

Park & Lee (2000) experimentally studied flows around finite cylinders with aspect ratios of 6, 10 and 13 at $Re = 2 \times 10^4$. The flow studied in the present paper is that of a cylinder with an aspect ratio of 6 from Park & Lee (2000). An investigation similar to that described in Park & Lee (2000) was presented in Park & Lee (2002). However, the experimental study reported in the latter deals more with the influence of various atmospheric boundary layers on flows studied earlier in the uniform flow in the former.

The flow with an aspect ratio of 6 was further investigated in Park & Lee (2004), where the influence of the free end corner shape on the surrounding flow was studied. The Reynolds number was decreased from $Re = 2 \times 10^4$ to 7500 for particle image velocimetry (PIV) investigations. The formation of the counter-rotating twin vortices in the case of the right-angled flat-tip free end (such as that studied in the present paper) was suggested in Park & Lee (2004) to be a result of the interaction between the entrained ambient fluid coming along the edge of the free end and the downwash fluid. Comparing different free end shapes, Park and Lee found that the downwash was stronger for the right-angled flat-tip free end compared to the radiused-tip free end.

Most numerical simulations are of short aspect ratio cylinders. Majumdar & Rodi (1989) made RANS simulations using a $k - \varepsilon$ turbulence model of the flow around a cylinder with an aspect ratio of $L/D = 1.9$ at $Re = 5 \times 10^6$. According to these authors, the poor agreement of the predictions was due to the coarse computational grid and the fact that unsteady effects could not be taken into account by the steady RANS simulation. This is understandable, keeping in mind the level of unsteadiness in finite cylinder flow.

Probably the first large eddy simulation (LES) of finite cylinder flow was by Fröhlich & Rodi (2004), who simulated a flow where $L/D = 2.5$ at $Re = 4.3 \times 10^4$. Although these LES predicted the main features of the flow, details of the flow on the cylinder's free end and near the ground were not predicted. This was attributed by the authors of Fröhlich & Rodi (2004) to the lack of resolution.

Lee, Lin & Friehe (2007) later made LES of the same flow as in Fröhlich & Rodi (2004). The difference between Lee *et al.* (2007) and Fröhlich & Rodi (2004) was that the former used a finite element code while the latter predicted the flow with a finite volume code. Furthermore, the computational grids and the near wall treatments were different. However, the LES by Lee *et al.* (2007), where the first grid point was between 7.7 and 30 wall units from the wall, was not able to resolve the near wall flow physics. The results reported in Lee *et al.* (2007) were similar to those in Fröhlich & Rodi (2004).

Pattenden *et al.* (2007) made LES and detached eddy simulation (DES) of their own experiment at $L/D = 1$ and $Re = 2 \times 10^5$. Although the agreement with the experimental data was better for DES than LES, both simulations were found to suffer from insufficient resolution.

Afgan, Moulinec & Laurence (2006) presented LES of the flows studied in Park & Lee (2000) where $L/D = 6$ and 10 and $Re = 2.0 \times 10^4$. Their simulation of the flow at the aspect ratio of $L/D = 6$ is particularly interesting for the purpose of the present work, as this is the flow that is examined in this paper. The grid in their simulation contained 1.8×10^6 computational nodes, with the first computation grid points at 1 and 5 wall units from the cylinder and the ground, respectively. While they did not report the resolution in the other two directions, they did note that the resolution is not sufficient for an accurate reproduction of the development of the boundary layer. The results of their simulation will be compared with the present results and discussed later in the paper.

The most recent numerical simulation is that by Palau-Salvador *et al.* (2010), who made LES of their own experimental cases with $L/D = 2.5$, $Re = 4.3 \times 10^4$ and $L/D = 5$, $Re = 2.2 \times 10^4$. They presented comparisons of the results for the velocities and turbulence stresses between their LES and experimental investigations. Their simulation for a short cylinder predicted the flow in rather good agreement with the experimental data, although the recirculation zone behind the cylinder was slightly overpredicted. On the other hand, their LES of the long cylinder predicted a flow with a different recirculation zone from the experimental one. Their LES recirculation zone was not only longer but also had a focus farther downstream from the cylinder than in the experimental data. In addition to reporting comparisons of the velocities and stresses, they presented streamlines projected on several planes and the surface of the cylinder. They later used the information from these figures to discuss the time-averaged flow structures. Beyond the time-averaged flow, snapshots of pressure fluctuations were given in Palau-Salvador *et al.* (2010) that showed the instantaneous flow structure.

The intension of the present work was to use LES to explore both the instantaneous and the time-averaged flows around a tall cylinder. The focus is not on using a new numerical technique but on using the information from a well-resolved simulation to describe the flow, compare the results with previous knowledge and, if possible, fill in the missing gaps. As mentioned, there are only a few numerical simulations of flows around tall cylinders and there are still open questions about parts of this flow. For example, the lower part of the near wake is not fully understood. There are also different theories about the time-averaged flow on and around the free end. In addition to these questions, the present work will explore the instantaneous flow mechanisms that are active for example in the formation of the tip vortices on the free end and the so-called downwash process in the near wake.
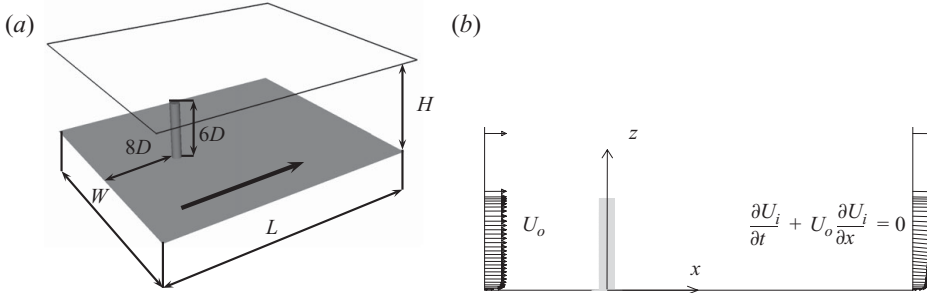
FIGURE 1. (*a*) Computational domain. (*b*) View from the lateral side of the computational domain.

2. Description of the set-up

The finite cylinder studied in this paper is that used in the experiments by Park & Lee (2002). The cylinder was mounted vertically on a flat plate. The free stream inlet velocity of $U_o = 10\,\mathrm{m\,s}^{-1}$ and diameter D equal to $0.03\,\mathrm{m}$ give a Reynolds number of approximately 2×10^4. Free-stream turbulence intensity in the test section was less than $0.08\,\%$ in the experiment (Park & Lee 2002). A test section of $24D \times 20D \times 28D$ (width $\times$ height $\times$ length) was used in the simulations (figure 1*a*). The inlet and outlet in the numerical wind tunnel are placed $8D$ and $19D$ from the cylinder, respectively.

3. Governing equations and subgrid-scale modelling

There are several different approaches to LES including the conventional and implicit LES. The most common is the conventional (or classical) LES where an explicit subgrid scale model is used to model the influence of the unresolved flow scales to the resolved ones. The implicit LES uses some upwind numerical schemes without the explicit addition of a subgrid scale model. In such implicit LES, the subgrid scale model is implicitly designed into the numerical scheme, based on the observation that an upwind scheme can be rewritten as a central differencing scheme plus a dissipative term (Drikakis *et al.* 2009). For reviewing the implicit LES, the author refers to Drikakis *et al.* (2009) and their application to complex flows (Hahn & Drikakis 2009*a,b*). The present work is an example of conventional LES.

The governing LES equations are the incompressible Navier–Stokes and the continuity equations filtered with the implicit spatial filter of characteristic width Δ (Δ is the grid resolution in this work):

$$\frac{\partial \bar{u}_i}{\partial t} + \frac{\partial}{\partial x_j}\left(\bar{u}_i \bar{u}_j\right) = -\frac{1}{\rho}\frac{\partial \bar{p}}{\partial x_i} + \nu \frac{\partial^2 \bar{u}_i}{\partial x_j \partial x_j} - \frac{\partial \tau_{ij}}{\partial x_j} \tag{3.1}$$

and

$$\frac{\partial \bar{u}_i}{\partial x_i} = 0. \tag{3.2}$$

Here, $\bar{u}_i$ and $\bar{p}_i$ are the resolved velocity and pressure respectively, and the bar over the variable denotes filtering.

These equations are derived applying a filtering operation

$$\bar{f}(x_i) = \int_\Omega f(x_i')G(x_i, x_i')\,\mathrm{d}x_i', \tag{3.3}$$

to the Navier–Stokes and the continuity equations. Here, G is a top hat filter function and Ω represents the entire flow domain. The filtered variables in the governing equations (3.1) and (3.2) are obtained implicitly through the spatial discretization.

The goal of the filtering is to decompose the fluid motion into a large-scale component that is resolved and a small subgrid scale (SGS) which is modelled. The influence of the small scales of the turbulence on the large energy carrying scales in (3.1) appears in the SGS stress tensor, $\tau_{ij} = \overline{u_i u_j} - \bar{u}_i \bar{u}_j$. The algebraic eddy viscosity model originally proposed by Smagorinsky (1963) is used in this paper for its simplicity and low computational cost. The Smagorinsky model represents the anisotropic part of the SGS stress tensor, τ_{ij}, as

$$\tau_{ij} - \tfrac{1}{3}\delta_{ij}\tau_{kk} = -2\nu_{sgs}\bar{S}_{ij}, \tag{3.4}$$

where $\nu_{sgs} = (C_s f \Delta)^2 |\bar{S}|$ is the SGS viscosity,

$$\bar{S}_{ij} = \frac{1}{2}\left(\frac{\partial \bar{u}_i}{\partial x_j} + \frac{\partial \bar{u}_j}{\partial x_i}\right) \tag{3.5}$$

is the resolved rate-of-strain tensor and $|\bar{S}| = (2\bar{S}_{ij}\bar{S}_{ij})^{1/2}$. f in the expression for the SGS viscosity is the van Driest damping function:

$$f = 1 - \exp\left(\frac{n^+}{25}\right), \tag{3.6}$$

where n is the wall normal distance. Using this damping function, wall effects are partially taken into account by 'damping' length scale $l = C_s \Delta$ near the walls. The value of $C_s = 0.1$ previously used for bluff-body flows (Krajnović & Davidson 2002), flow around a simplified bus (Krajnović & Davidson 2003) and flow around a generic car called the Ahmed body (Krajnović & Davidson 2005) is used in this work. The filter width Δ, is defined in this work as $\Delta = (\Delta_1 \Delta_2 \Delta_3)^{1/3}$, where Δ_i are the computational cell sizes in the three coordinate directions.

4. Boundary conditions and numerical details

The average turbulent intensity at the inlet of the wind tunnel used in the experiments of Park & Lee (2002) was low (less than 0.08 %). A uniform velocity profile, U_∞, constant in time, was thus used as the inlet boundary condition in the present LES. The boundary layer thickness of 2 mm (corresponding to approximately 7 % of the cylinder's diameter at the location of the cylinder, $x = 0$) found in the experiment at the position of the cylinder was obtained in the simulation by prescribing the appropriate distance between the inlet and the cylinder. The resolution of the boundary layer on the ground would require very large computer resources and the boundary layer on the ground used in the present LES is only an approximation having the same boundary layer thickness as the one used in the experiment. This will of course have influence on the flow structures near the ground. However, the boundary layer is very thin and was found not to influence the flow in the upper regions of the cylinder in the experimental study by Park & Lee (2000). The convective boundary condition $\partial \bar{u}_i/\partial t + U_\infty(\partial \bar{u}_i/\partial x) = 0$ was used at the downstream boundary. The lateral surfaces and the ceiling were treated as slip surfaces using symmetry conditions ($\partial \bar{u}/\partial y = \partial \bar{w}/\partial y = \bar{v} = 0$ for the lateral sides and $\partial \bar{u}/\partial z = \partial \bar{v}/\partial z = \bar{w} = 0$ for the ceiling). No-slip boundary conditions were used on the surface of the body and instantaneous wall functions based on the log-law (see Krajnović & Davidson 2003 for details) were applied on the channel floor.
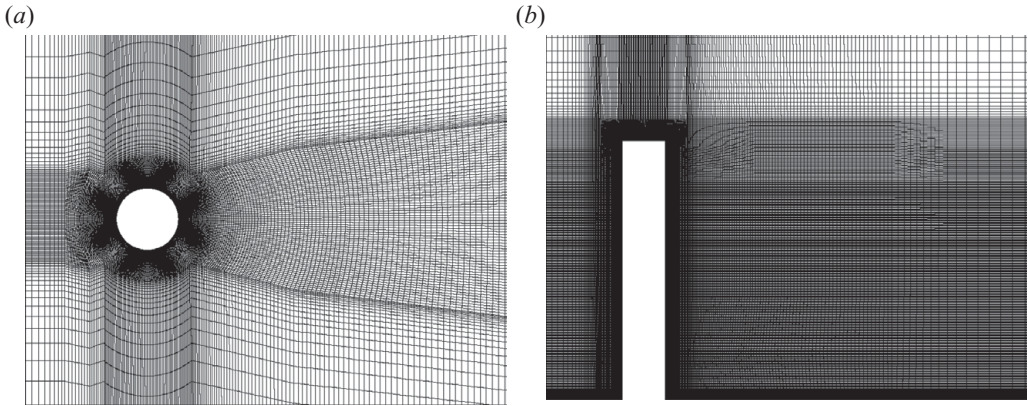
(a)

(b)

FIGURE 2. (a) Computational mesh. (a) View from above a plane $z = 3D$. (b) View from a side of plane $y = 0$.

Accuracy was established by making three LES on different computational grids containing 7, 13.5 and 21.5 million nodes. Filtering of the equations in the present work was done using computational grid with the filter width related to the dimensions of the computational cells. Furthermore, the subgrid-scale model contains the filter width which varies with the size of the computational cells. Thus, the numerical error could not be isolated from the model error, and only the mixture of the two errors was studied in the grid convergence study. Three multi-block hexahedral meshes were used in the simulations. A grid topology was constructed using several O and C grids in order to concentrate most on the computational cells close to the cylinder (figure 2). A large number of cells close to the surface is needed in order to resolve the laminar boundary layer on the front part of the cylinder.

The fine and medium computational grids have a wall normal resolution of $n^+ < 0.3$, $12 < \Delta s^+ < 25$ in the streamwise direction and $3 < \Delta l^+ < 20$ in the direction parallel to the surface of the body and normal to the streamwise direction (the mean Δl^+ is around 10). This resolution is valid over the entire cylinder except at the free end where n^+ locally reaches 1.5 (figure 3). Here, $\Delta n^+ = \Delta n \langle u_\tau \rangle_t / \nu$, $\Delta s^+ = \Delta s \langle u_\tau \rangle_t / \nu$, $\Delta l^+ = \Delta l \langle u_\tau \rangle_t / \nu$ and $\langle u_\tau \rangle_t$ is the time-averaged friction velocity. The contribution of the subgrid-scale stresses in the region around the cylinder is small. This is reflected by the ratio of the subgrid-scale to the laminar viscosity which was found to be $\nu_{sgs}/\nu \leqslant 1$, very near to the cylinder and in the shear layer separating from the cylinder. The near wake region behind the cylinder has $1 \leqslant \nu_{sgs}/\nu \leqslant 5$. The time step $dt^* = dt U_\infty / D$ was 1.33×10^{-3}, 1×10^{-3} and 8.3×10^{-4} in the coarse, medium and fine grids, respectively, giving a maximum CFL number of approximately 0.7. All simulations were first run during the time $t^* = t U_\infty / D = 112$ corresponding to the four flow through passages through the tunnel. Afterwards, the flow was averaged during $t^* = 233$ (280, 000 time steps for the fine grid LES).

5. Numerical method

Equations (3.1) and (3.2) are discretized using a 3D finite volume method for solving the incompressible Navier–Stokes equations using a collocated grid arrangement (Davidson & Farhanieh 1995). Both convective and viscous plus subgrid fluxes are approximated by central differences of second-order accuracy. The time integration is done using the second-order Crank–Nicolson scheme. Although no explicit dissipation
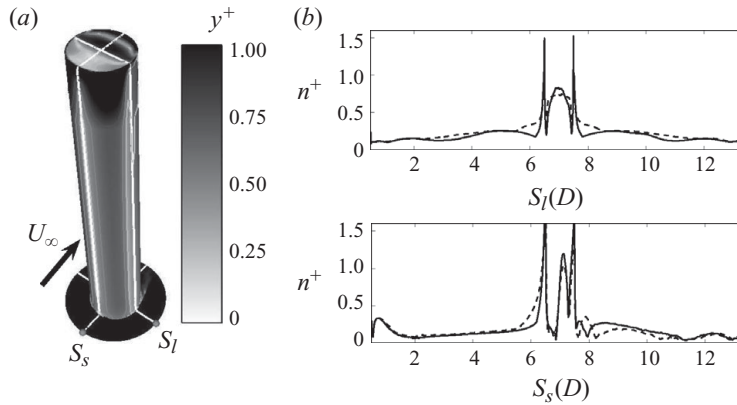
FIGURE 3. (*a*) Wall normal resolution of the medium cylinder on the surface of the cylinder. (*b*) Wall normal resolution along lines S_s and S_l in (*a*). Solid and dashed lines correspond to fine and medium grids, respectively. Note that lines S_s and S_l do not start at the points in (*a*) but at the point of the attachment of the cylinder on the ground.

is added to prevent odd–even decoupling, an implicit dissipation is present. This is done by adding the difference between the pressure gradient at the face and the node. It can be shown that this term is proportional to the third derivative of pressure, i.e. $\partial^3 p/\partial x_i^3$. This term corresponds to Rhie–Chow dissipation (Rhie & Chow 1983). The SIMPLEC algorithm was used for the pressure–velocity coupling. The code was parallelized using block decomposition and the MPI message passing system (Nilsson & Davidson 1998).

Usage of second-order accurate numerical scheme is most common in the engineering applications of LES. There are however some recent studies that have used higher-order methods both for classical and implicit LES (Hahn & Drikakis 2009*a,b*). A review of the usage of higher-order methods is presented in (Drikakis *et al.* 2009).

6. Results

6.1. *Comparison with the experimental data*

The time-averaged results of the present LES were compared with the existing experimental data (Park & Lee 2002) at several different positions in the domain. Surface pressure coefficients at four positions along the cylinder are compared with the experimental data from (Park & Lee 2002) in figure 4. The angle zero degrees in figure 4 corresponds to the upstream stagnation point ($x/D = -0.5$, $y/D = 0$) and increases in the clockwise direction to $180°$ at the rear stagnation point ($x/D = 0.5$, $y/D = 0$).

The agreement of the present LES profiles of C_p with the experimental data is good. As seen in figure 4, the C_p values decrease in both the experimental data (Park & Lee 2002) and in our medium and fine grid simulations as we move towards the free end of the cylinder. This is consistent with the change of the flow around the cylinder due to the flow above the free end and the downwash just behind it. Another observation is that the two LES using the medium and fine computational grids produce similar results, proving that sufficient resolution was achieved. Park & Lee (2002) reported the velocity profile in the wake at $z/L = 0.5$ and $x/D = 5$. Their measurements were
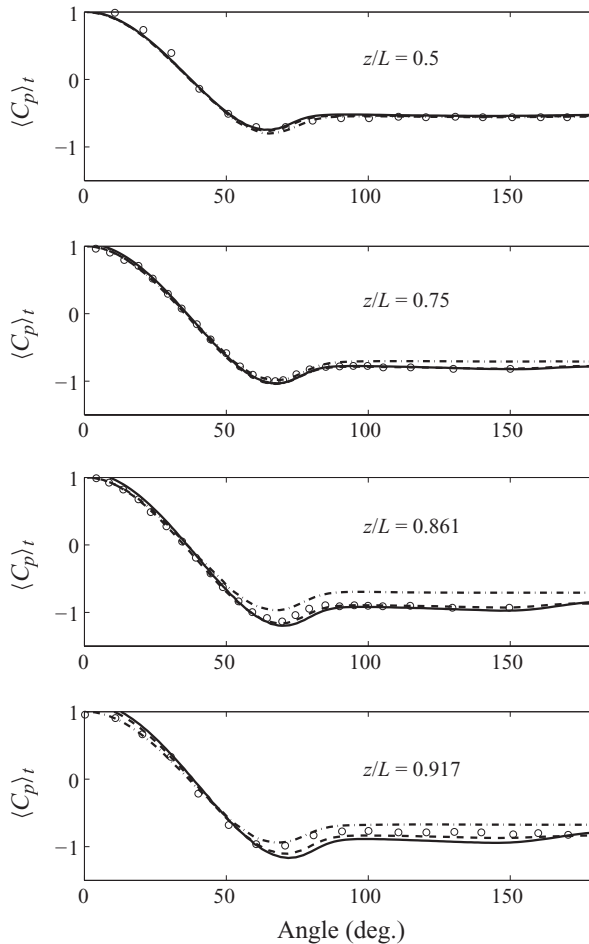
FIGURE 4. Surface pressure coefficient at four z locations. Solid line: fine grid LES; dashed line: medium grid LES; dashed-dotted line: coarse grid LES; circles: experiments by Park & Lee (2002).

made using hot wire, which is not an accurate technique in highly turbulent near wake flow behind the cylinder. Thus it is not clear how accurate these data are, but as they are the only velocity data available, they were used in the present study for comparison with our LES.

Figure 5(*a*) shows a comparison of the present LES results for velocity profiles at $z/L = 0.5$ and $x/D = 5$. The medium and the fine grid LES predicted the velocity profile, which is almost identical but has a much lower minimum than the experimental profile. The coarse grid simulation predicted a slightly wider profile with approximately the same minimum as the two finer grid simulations. The streamwise turbulence intensity at the same position is presented in figure 5(*b*). Although all three LES produce results in good agreement with the experimental data, the grid refinement improves the agreement with the same results for the medium and the fine grid LES. All three LES and previous DES (personal communication M. Strelets 2005) and LES (Afgan *et al.* 2006) results have a dip around position $y/L = 0$, which is different from the experimental data. Both results for the velocity and turbulence intensity, with a lower minimum velocity and a dip in the turbulence intensity in the
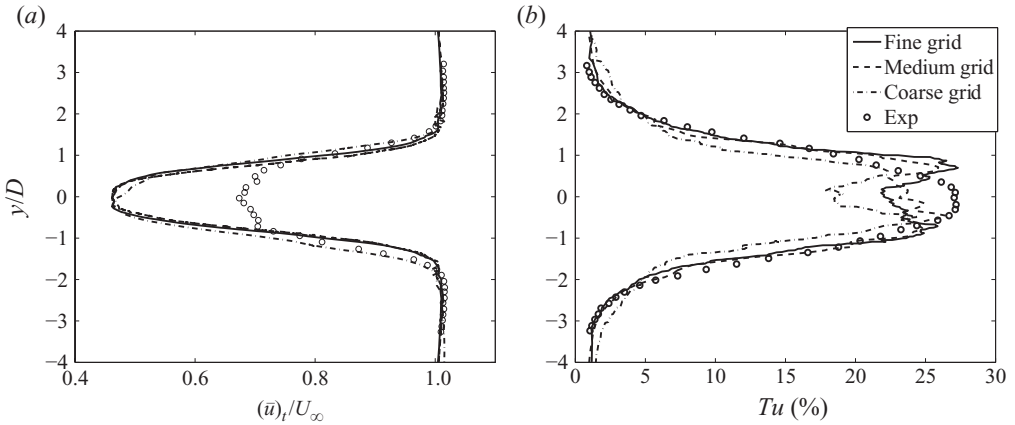
FIGURE 5. (a) Streamwise velocity profiles. (b) Resolved turbulence intensity in the streamwise direction at position $z/L = 0.5$, $x/D = 5$. Solid line: fine grid LES; dashed line: medium grid LES; dashed-dotted line: coarse grid LES; symbols: experiments by Park & Lee (2002).
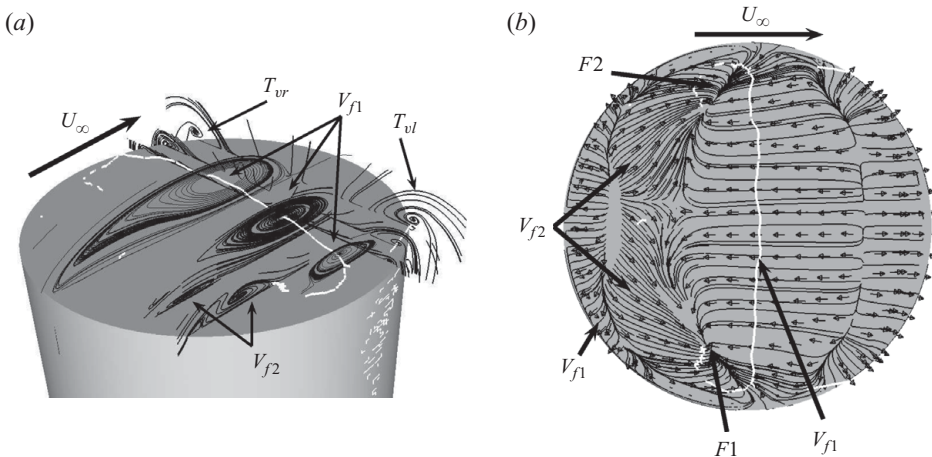

FIGURE 6. (a) Streamlines projected on several y and x planes. (b) Particle traces on the surface of the free end and velocity vectors just above the free end. The velocity vectors are not to scale for clarity. T_{vr} and T_{vl}, tip vortices; V_{f1} and V_{f2}, recirculating regions, see main text for further explanation; $F1$ and $F2$, focal points 1 and 2.

present LES, are in agreement with the previous LES (Afgan *et al.* 2006) and DES (personal communication M. Strelets 2005).

6.2. *Flow around the free end*

The flow around the free end of the cylinder has been studied by several authors (Kawamura *et al.* 1984; Roh & Park 2003; Park & Lee 2004; Pattenden, Turnock & Zhang 2005; Hain, Kähler & Michaelis 2008; Palau-Salvador *et al.* 2010). This section will explore the free end flow resulting from the present LES and compare it with previous observations. Figure 6(a) shows the streamlines projected on several y and x planes. Furthermore, vortex cores were calculated using EnSight post-processing software, which uses algorithms based on techniques outlined by Sujudi & Haimes (1995). Additional information about the structures is provided in figure 6(b), where
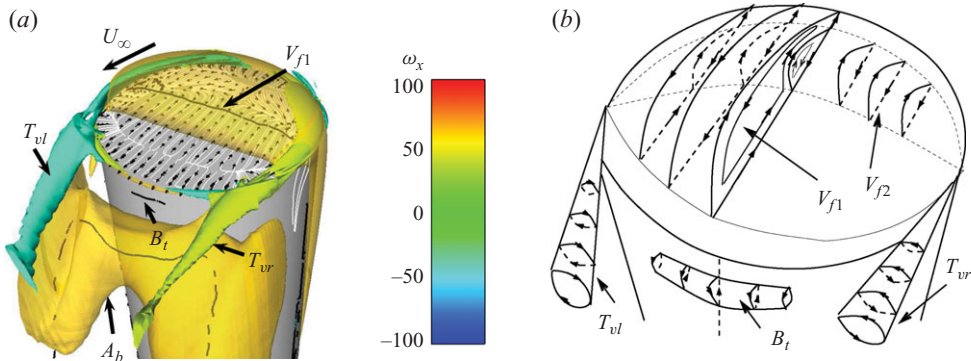
FIGURE 7. (Colour online available at journals.cambridge.org/FLM) (*a*) Isosurface of streamwise component of vorticity $\omega_x = \pm 40$ showing the tip vortices and an isosurface of low static pressure showing the arch vortex system A_b. The tip vortices are coloured with ω_x. (*b*) A sketch of the time-averaged vortex system on and around the free end of the cylinder. The size of the flow structures is not to scale.

streamlines are projected onto the surface of the cylinder's end. Isosurfaces of the streamwise vorticity component, ω_x, and low pressure are shown in figure 7(*a*). A summary of the time-averaged flow near the free end is presented in the sketch in figure 7(*b*). The flow on the top surface contains tip vortices T_{vr} and T_{vl}, the large recirculating region V_{f1} originating at the leading edge of the cylinder and reattaching at approximately $0.82D$ in the x direction and plane $y = 0$ and secondary recirculation region V_{f2}. The recirculation region, V_{f2}, is a result of separation of the recirculating flow from V_{f1} on its way back to the leading edge. Note that the recirculating region, V_{f2}, does not stretch all the way to the leading edge of the cylinder but reattaches and the V_{f1} region takes over. This flow picture has many similarities with that found by Palau-Salvador *et al.* (2010). For example, both recirculation regions V_{f1} and V_{f2} can be derived from streamline pictures presented in (Palau-Salvador *et al.* 2010). Furthermore, the V_{f2} structure was found to be very thin both in the work of Palau-Salvador *et al.* (2010) and the present work (not shown here). Roh & Park (2003) suggested that two vortices originate from two focal points, $F1$ and $F2$ in figure 6(*b*), and bend over to form streamwise vortices. Previous investigations by Pattenden *et al.* (2005) and Palau-Salvador *et al.* (2010) and the present work prove that this is not the case. Kawamura *et al.* (1984) suggested the existence of a mushroom vortex at the position of vortex V_{f1}. Pattenden *et al.* (2005) suggested that the vortex core of V_{f1} is attached to the free end at two focal points, F1 and F2. Figure 6(*b*) shows that this is the case, proving both the assumption of Pattenden *et al.* (2005) and Kawamura *et al.* (1984).

In addition to the larger vortices, V_{f1} and V_{f2}, Palau-Salvador *et al.* (2010) suggested the existence of one more very small vortex near the leading edge and lifted further away from the surface. However, the present work and PIV studies by Hain *et al.* (2008) and Park & Lee (2004) give no indication of such a structure.

Tip vortices T_{vr} and T_{vl} visualized in figure 7 as isosurfaces of the streamwise vorticity component $\omega_x = \pm 40$ have been observed in the time-averaged flow in several previous studies. Similar to the findings of Hain *et al.* (2008) and Pattenden, Turnock & Bressloff (2002), the present work also shows that the tip vortices exist only in the time-averaged flow. The instantaneous flow contains smaller coherent structures that change over time. However, figure 8(*b*) shows that the instantaneous structures have
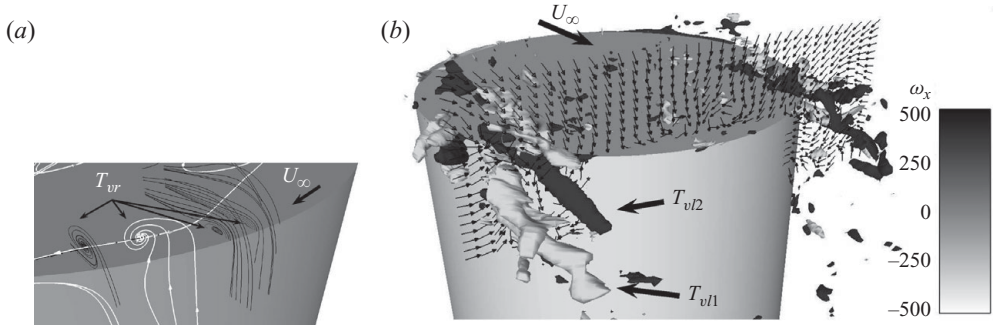
FIGURE 8. (a) Time-averaged streamlines projected in streamwise (x) planes (shown in black). White streamlines are three-dimensional. (b) Two instantaneous streamwise vorticity component $\omega_x = \pm 500$ isosurfaces. Velocity vectors are in plane $x = 0.45D$.

a dominant direction of rotation identical to that of the time-averaged tip vortices. Hain *et al.* (2008) concluded from their PIV measurements at positions $x/D = 0.5$ and $y/D = \pm 0.5$ that two instantaneous vortices can be seen at the position of each time-averaged tip vortex. Figure 8(*b*) shows that the counter-rotating instantaneous vortices suggested in Hain *et al.* (2008) exist in the present work. The outer instantaneous vortex, such as T_{vl1} on each side, is always stronger however, and this is the reason why the time-averaged tip vortices have the same sense of rotation as in e.g. T_{vl1}.

The tip vortices are formed from the interaction of the Kármán flow along the upper part of the cylinder and the flow over the free end. Figure 8(*a*) shows how the flow rises over the edge of the free end and swirls into the tip vortex, T_{vr}. As seen in figure 7(*a*), the tip vortices are influenced by the downwash flow and therefore point slightly towards the ground in agreement with the observation of Park & Lee (2002, 2004). Similar observations were made for tip vortices on a short cylinder in Pattenden *et al.* (2005).

6.3. *The horseshoe vortex system*

The impingement of the flow at the bottom of the cylinder results in a main horseshoe vortex, H_1, and a secondary horseshoe vortex, H_2 (figure 9). The two vortices have different direction of rotation, as seen in figure 9(*c*). The centre of the main and the secondary horseshoe vortices is at $x/D = -0.68$, $z/D = 0.05$ and $x/D = -0.58$, $z/D = 0.16$, respectively. A vortex H_3 was found in front of the main vortex (figure 9*d*). This is in agreement with the topology of the horseshoe vortex system that was suggested by Baker (1980) and found earlier in Pattenden *et al.* (2005). However, similar to Pattenden *et al.* (2005), a third thin vortex between H_1 and H_3 (suggested by Baker 1980) was not found in the present work probably due to the too coarse wall normal resolution (with respect to the wall normal extension of such a third vortex) on the ground. The instantaneous horseshoe vortices are unsteady and move in all three spatial directions (figure 10). A rather complete horseshoe vortex can be observed at some time instances, whereas the structures break into several parts at other times. This is in agreement with the observations of Pattenden *et al.* (2005), who studied the change of the horseshoe vortex in the symmetry plane in time. One important observation in the present work is that the instantaneous structures, which averaged into the main horseshoe vortex H_1, move rather far in the y direction (figure 10*b*).
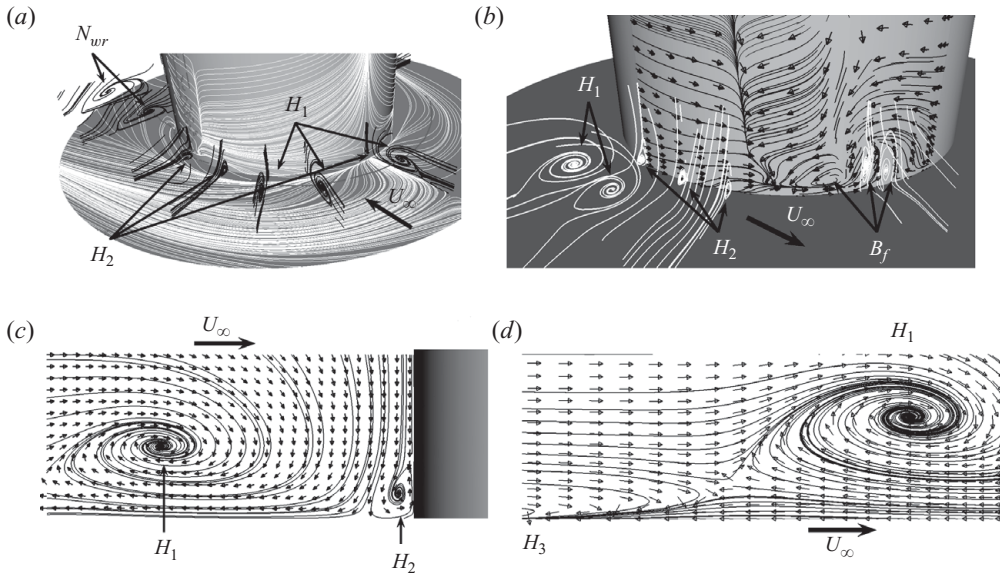
FIGURE 9. Time-averaged flow. (*a*) Streamlines projected on several planes together with vortex cores and trace lines of the surfaces show the time-averaged horseshoe vortices. (*b*) Streamlines projected on several planes (white) and trace lines on the surface of the cylinder. (*c–d*) Streamlines and velocity vectors projected on symmetry plane $y = 0$ in front of the cylinder.
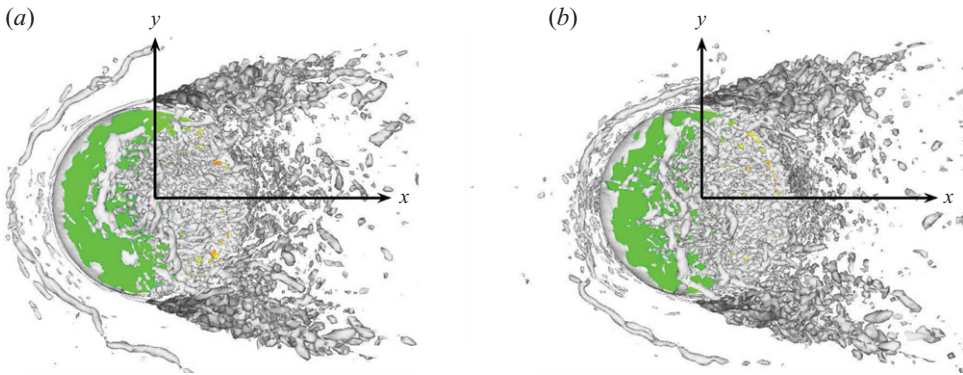

FIGURE 10. (Colour online) Instantaneous horseshoe vortices visualized using an isosurface of $Q = 130\,000$. Figures (*a*) and (*b*) show the time position of zero and minimal (i.e. in the negative y direction) side force. View from above the cylinder.

H_2 exists approximately until the line of flow separation on the cylinder at an angle of about $60°$ from the upstream stagnation point (figure 9*b*). The flow on the cylinder's surface near the ground is dominated by the main horseshoe vortex, H_1, until the separation curve, where the near wake flow takes over. The flow from both sides of the separation curve points towards it and downwards, resulting in the imprint of vortex B_f on the surface of the cylinder in figure 9(*b*). As the horseshoe vortex prevails further away from cylinder, vortex B_f stretches from the surface of

(*a*)   (*b*)
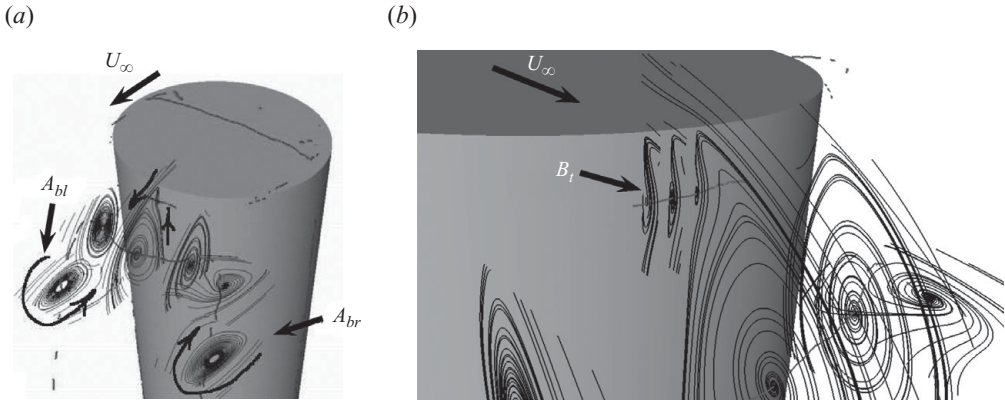

FIGURE 11. Upper part of the near wake displayed using streamlines projected
on planes and vortex cores.

the cylinder a short distance downstream and soon dies out as a result of the strong
backflow close to the symmetry plane and the influence of vortex N_w (one leg N_{wr}
of vortex N_w is visible in figures 9*a* and 12*a*.). Vortex B_f exists on both sides of the
cylinder's symmetry plane and was previously observed in Pattenden *et al.* (2005) and
Palau-Salvador *et al.* (2010). The direction of rotation of B_f is the same as that of
H_2, transporting the flow from the ground plane up along the cylinder, followed by a
pushing of the flow away from the cylinder.

6.4. *Near-wake flow*

Previous works by Pattenden *et al.* (2007) and Fröhlich & Rodi (2004) among others
show that the near wake behind a short finite cylinder is dominated by an arch vortex
attached to the ground surface by its legs. The present work shows that the arch vortex
behind a longer cylinder has legs A_{bl} and A_{br} inclined in the streamwise direction
with respect to the cylinder axis (figure 12). The angle of inclination of the cylinder
studied in the present work was found to be approximately $31°$. A similar observation
of inclined legs of the arch vortex was made by Sumner, Heseltine & Dansereau
(2004) for a cylinder with aspect ratios of 5, 7 and 9. This is understandable, as the
downwash flow from above the cylinder's top is strong only behind the upper half
of the cylinder, while the lower part of the flow behind the cylinder is dominated
by the streamwise flow and Kármán vortices. Figure 11(*a*) shows the near wake flow
close to the cylinder's free end. The spatial distribution of the structures forming
the arch vortex is exposed using streamlines projected on several planes. A closer
look at figure 11(*b*) shows the existence of vortex B_t just below the cylinder's free
end. As seen in figure 12(*b*), the flow in the symmetry plane moves towards the
cylinder near the ground and bends down after the stagnation point, forming the
N_w vortex. The focus of this structure moves away from the cylinder and upwards
as we move in the *y* direction (figure 14). At approximately $x/D = 1.38$, $y = \pm 0.32$
position , the vortex bends as a result of the interaction with the streamwise flow and
stretches in the streamwise direction. Figure 15 shows that, while the lower part of
the near wake is dominated by the downwash very close to the cylinder, the upwash
dominates further downstream. This is a result of the two legs, N_{wl} and N_{wr}, rotating
in counter-clockwise and clockwise directions, respectively. As a result of their counter
rotation, the two legs of vortex N_w move up (in the positive *z* direction) and away
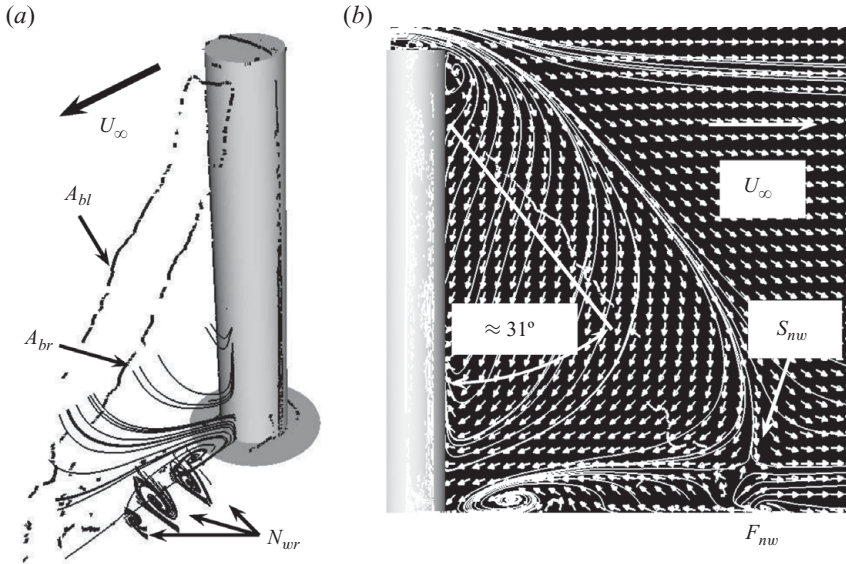
FIGURE 12. (*a*) Vortex cores and streamlines projected on symmetry plane $y = 0$ and three x planes behind the cylinder. (*b*) Near wake visualized with vortex cores and streamlines and velocity vectors in plane $y = 0$. The velocity vectors are not to scale for clarity.

from each other in the y direction as they stretch further away in the streamwise direction (figure 15). The findings here agree with those of Sumner *et al.* (2004). They also observed that the downwash weakens and goes over to upwash along the axis of the cylinder towards the base. For cylinders with aspect ratios of 5, 7 and 9, they found what they called *a base vortex pair* close to the ground plane, similar to the N_w vortex pair found in the present work. However, the cylinders in Sumner *et al.* (2004) were immersed in thick boundary layers (compared to the rather thin boundary layer in the present work), resulting in vortices of different sizes and positions compared to those in the present paper. Similar vortices were also observed by Tanaka & Murata (1999).

In the symmetry plane downstream of vortex N_w, a focus, F_{nw}, and a saddle point, S_{nw}, are visible in figures 12(*b*) and 13, indicating the closure of the separation region in the near wake. The interaction of the instantaneous structures that average to A_{bl}, A_{br}, N_{wl} and N_{wr} seems to be rather unsteady, as the vortex cores are difficult to separate in this region in figure 12(*a*) despite a very long averaging time.

6.5. *Far wake flow*

The time-averaged flow turning in along the cylinder interacts with the downwash flow beyond the closure of the separation bubble (after saddle point S_{nw} in figure 12) resulting in the flow in the symmetry plane impinging on the ground plane. After the impingement, the flow is pushed in outward directions away from the symmetry plane to form the two counter-rotating vortices shown in figure 16. The rotation direction of these vortices is the same as that of the tip vortices and the legs of the main horseshoe vortex, H_1, but opposite to that of N_{wr} and N_{wl}. Their vortex cores move up in the positive z direction, similar to what was found in Tanaka & Murata (1999).

A sketch of the time-averaged flow structures in the present LES is given in figure 17. This flow picture shows only the flow in the mean and is based on the time average of the instantaneous flow that is discussed in the previous sections.
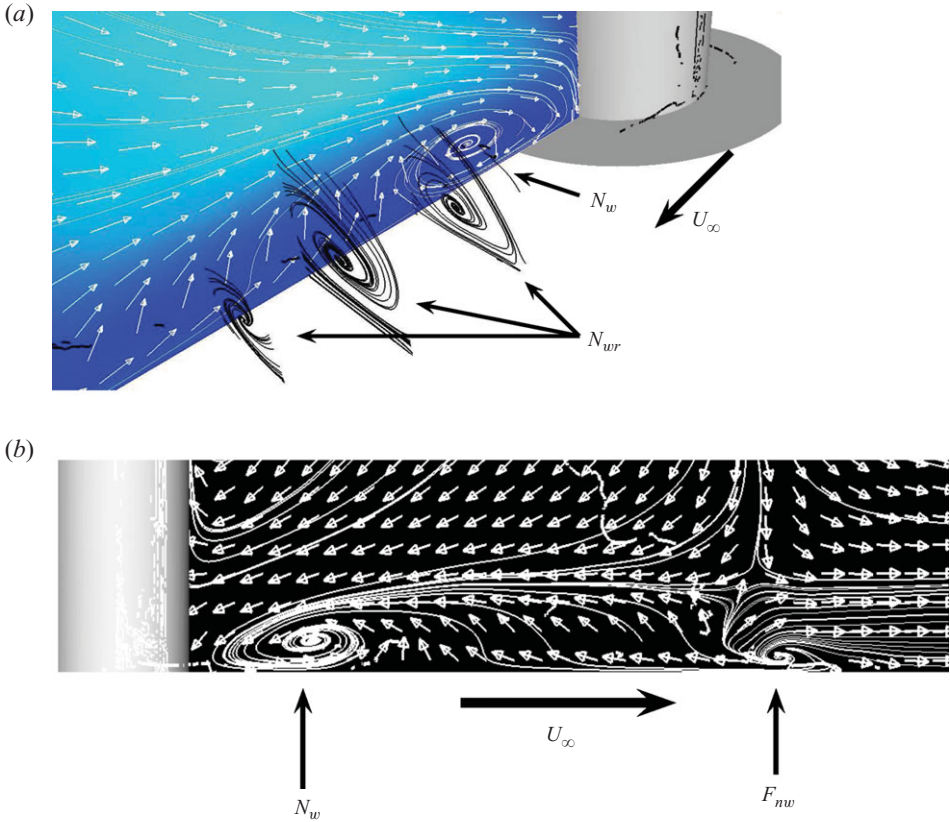
(*a*)

(*b*)

Figure 13. (Colour online) Streamlines and velocity vectors in the lower part of the near wake.

(*a*)   (*b*)
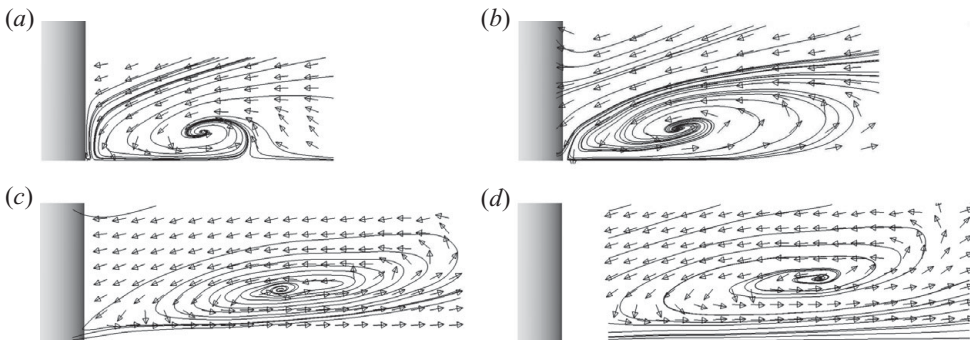
(*c*)   (*d*)

Figure 14. Vortex N_w visualized using time-averaged streamlines and velocity vectors projected on planes (*a*) $y = 0$, (*b*) $y = 0.25D$, (*c*) $y = 0.43D$ and $y = 0.47D$. Velocity vectors are not in the actual computational grid but are shown in a very coarse uniform grid for clarity.

6.6. *Instantaneous flow*

Figure 18 shows instantaneous flow structures around the cylinder. Thin vortices similar to those resulting from Kelvin–Helmholtz instability are formed along the cylinder (K-H in figure 18). Kelvin–Helmholtz instability can occur when velocity
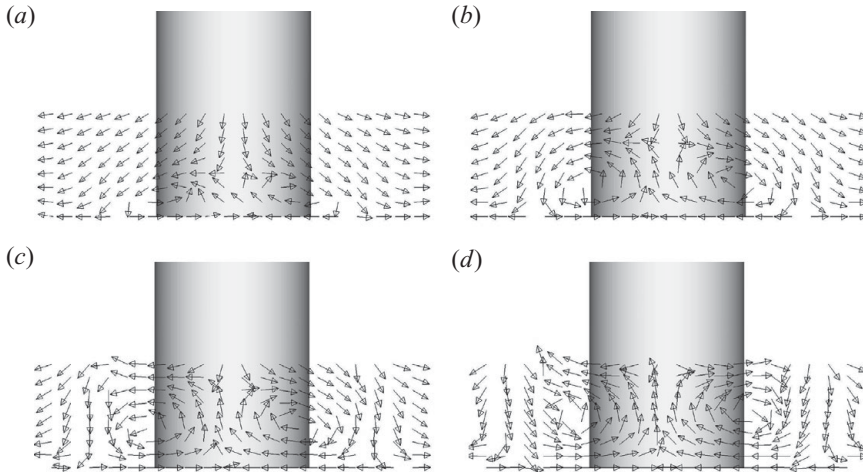
(*a*)

(*b*)

(*c*)

(*d*)

FIGURE 15. Time-averaged velocity vectors projected on planes (*a*) $x = 1.4D$, (*b*) $x = 2D$, (*c*) $x = 2.33D$ and (*d*) $x = 2.67D$. Velocity vectors are not in the actual computational grid but are shown in a very coarse uniform grid for clarity.
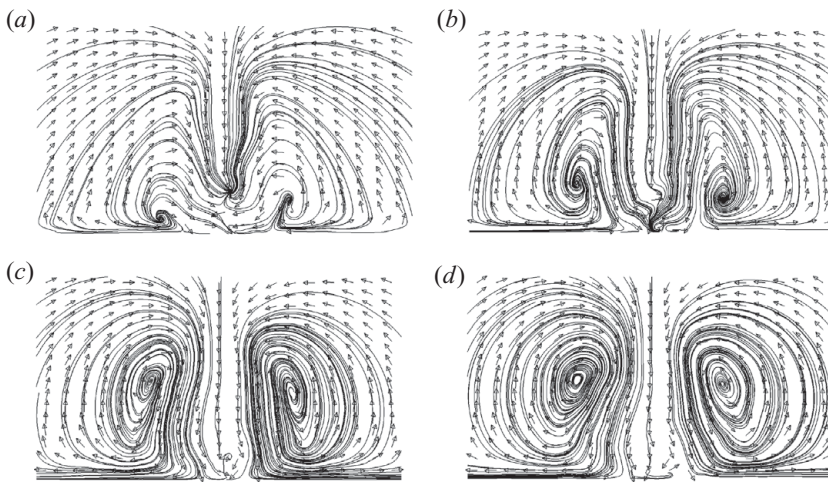
(*a*)

(*b*)

(*c*)

(*d*)

FIGURE 16. Time-averaged streamlines and velocity vectors projected on planes (*a*) $x = 2.28D$, (*b*) $x = 7.94D$, (*c*) $x = 9.61D$ and $x = 11.28D$. Velocity vectors are not in the actual computational grid but are shown in a very coarse uniform grid for clarity.

shear is present within a continuous fluid, and this is what happens here. The K-H vortices are a result of the roll-up of the transition waves into the discrete eddies along the shear layer before they become turbulent. Figures 18 and 19 show that the Kelvin–Helmholtz vortices are inclined in the streamwise direction near the free end of the cylinder. As suggested by Luo *et al.* (1996), the separated flow coming from the free end interacts with the separated flow along the cylinder and delays the separation (see figure 18). This explains the much higher pressure coefficient in the upper part of the lee side of the cylinder (figure 4).
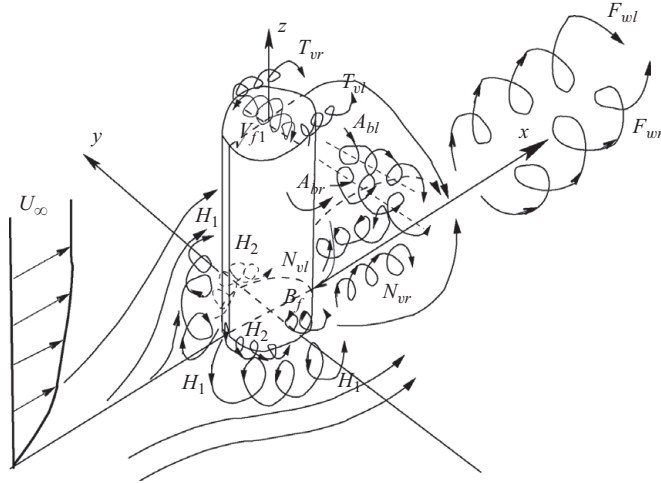
FIGURE 17. Sketch of the time-averaged flow configuration from the present LES.
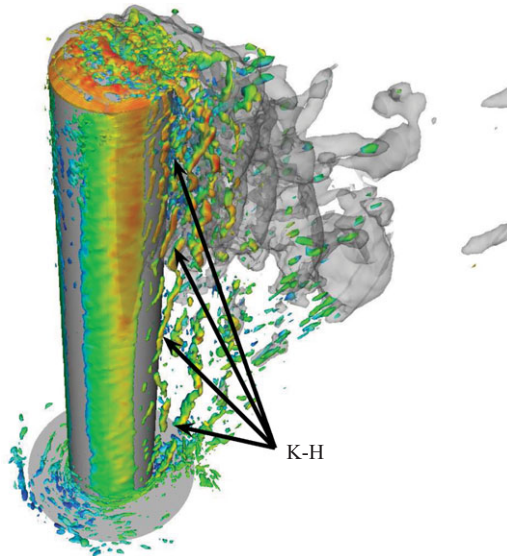

FIGURE 18. (Colour online) Instantaneous flow from LES using fine mesh. An isosurface of the second invariant of the velocity gradient Q coloured with velocity magnitude and an isosurface of pressure coloured grey.

6.6.1. *Vortex shedding*

An experimental investigation by Park & Lee (2002) revealed a vortex shedding frequency at 47 Hz corresponding to a dimensionless frequency of $St = 0.141$ (for an inlet velocity of $10\,[\mathrm{m\,s^{-1}}]$). This frequency was measured in the experiments at $x/D = 3$, $y/D = 2$ and $z/L = 0.5$ which are in the vicinity of the time-averaged shear layer. The turbulence intensity at this location was only a few per cent. This position is not in the near wake but is shifted in the spanwise direction, (y direction), and the hot wire anemometry technique used in the experiments is reliable in this region because of the low turbulence intensity.
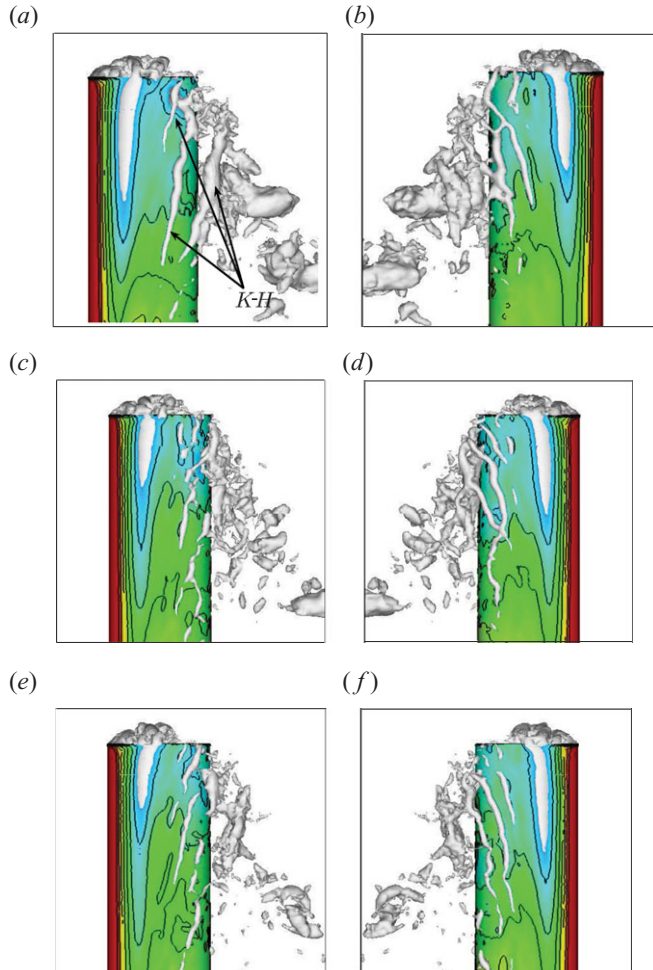
(*a*)

(*b*)

(*c*)

(*d*)

(*e*)

(*f*)

FIGURE 19. (Colour online) An isosurface of the instantaneous static pressure $p = -0.65$. Figures *a–b*, *c–d* and *e–f* show the time positions of minimal, zero and maximal side force, respectively. Left and right figures for each positions are views from negative and positive y directions, respectively. The cylinder is coloured with the static pressure.

The side force in time was monitored in the present LES and its time history was used to compute the power spectral density shown in figure 20. The results shown in this figure are from the simulation using the medium and the fine computational grids. Figure 20 shows that the medium and fine grids resulted in very clear vortex shedding frequencies at $St = 0.148$ and $St = 0.149$, respectively. Larger differences in frequency between LES using these two grids were found for low frequencies. The process of periodic increase and decrease of the side force was studied and is illustrated in figure 19. As seen in this figure, the negative and positive values of the side force are the result of the increase and decrease of the surface pressure on the lateral sides of the cylinder. For example, the negative value (in the y direction) of the side force is a result of the low pressure region shown in figure 19(*a*) and relatively high pressure on the opposite side, shown in figure 19(*b*). Figures 19(*e*) and (*f*) show the flow structures and the resulting surface pressure for the maximal positive (in
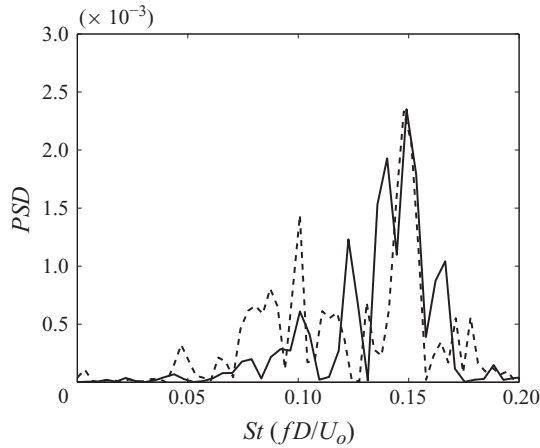
FIGURE 20. Power spectral density (PSD) distribution of the side force component signal. Fine grid (solid line); medium grid (dashed line).
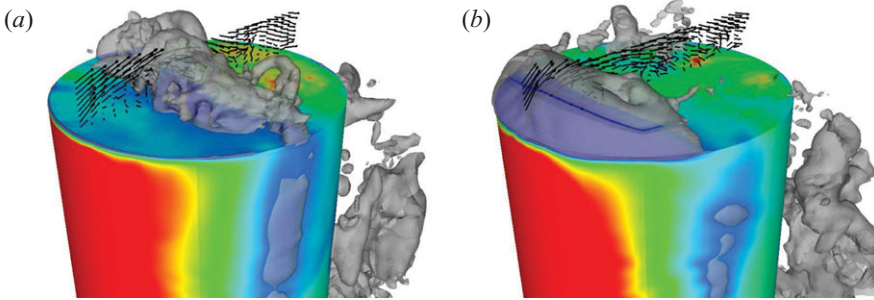

FIGURE 21. (Colour online) Two-flow time instances resulting in (*a*) high and (*b*) low lift force from medium grid LES. The grey surface in the figure is an isosurface of the static pressure $p = -0.7$ while the cylinder surface is coloured with the static pressure. The velocity vectors are shown in the symmetry plane ($z = 0$) above the free end. The time difference between the two positions is $\Delta t_* = \Delta t U_o / D = 0.5$. The view is from the windward side.

the *y* direction) side force, while figures 19(*c*) and (*d*) show the corresponding flow structures for zero side force.

In addition to monitoring the side force, we also monitored the drag force (in the *x* direction) and the lift force (in the *z* direction). Figure 21 shows the flow resulting in high (figure 21*a*) and low (figure 21*b*) lift force. As seen in these figures, the variation in the lift force is correlated with the two modes in the development of the flow structures above the free end. The formation of the separation region shown in figure 21(*a*) results in a large region with low pressure that pulls the cylinder in the positive *z* direction and thus produces a large lift force. After some time, the shear layer encloses this recirculation region and a coherent structure is formed (figure 21*b*) that moves to the approximate position of the middle of the free end ($x = 0$). Here, the smaller area of the free end is influenced by the low pressure from the vortex while there are more and larger high pressure spots on the rear of the free end than in figure 21(*a*). All this produces a lower lift force.
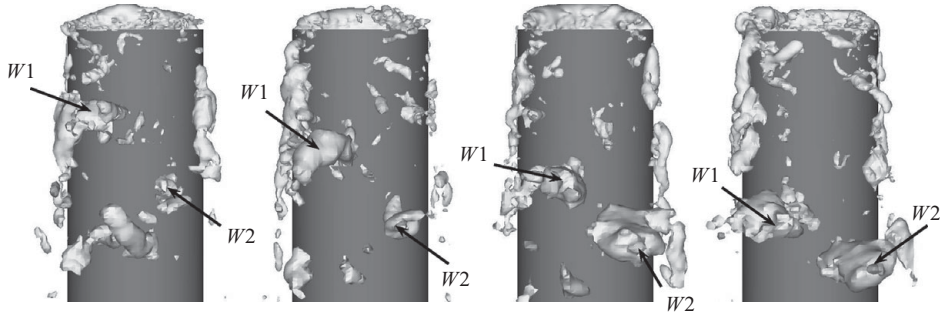
FIGURE 22. Isosurface of static pressure $p = -0.7$ from the fine grid. The time difference between two pictures is $\Delta t_* = \Delta t U_o / D = 4.6$. The view is from behind the cylinder.

6.6.2. *Downwash flow*

It was discussed earlier in the paper that two counter-rotating tip vortices in the time-averaged flow bend down behind the cylinder. This is a result of the flow processes in the instantaneous flow, where flow structures from figure 8(*b*) start to descend towards the ground, forming a downwash process. Figure 19 shows the flow structures seen from the side, which indicates that the downwash process occurs at an angle of approximately 31° with respect to the cylinder's symmetry axis.

The instantaneous downwash process can be followed in figure 22. Here we can follow two coherent structures, $W1$ and $W2$, that are formed from the interaction between the flow structures coming from above the free end and the vortices shed from the lateral sides of the cylinder.

6.6.3. *Far wake flow*

The alternate eddies in the far wake take the form of half arches with their base on the channel floor. These vortices are visible only after approximately $3.5D$ behind the cylinder. This is similar to vortices behind a stationary pile subjected to tidal flow presented in Zdravkovich (1997). They are convected downstream and are strong even 15 cylinder diameters behind the cylinder (figure 23). Two observations can be made from this figure: the distance between the subsequent vortices is relatively constant and the flow structures at the same x position are coherent (figures 23*a* and 23*b*) sometimes and disperse otherwise (figures 23*c* and 23*d*).

6.7. *Comparison with earlier LES*

Afgan *et al.* (2006) presented LES of two flows from the experimental studies by Park & Lee (2000) that had aspect ratios of 6 and 10. As their results with the shorter cylinder are relevant for the present work, they will be briefly discussed here. The comparison of the LES results (Afgan *et al.* 2006) with the experimental data in Park & Lee (2000) contains C_p profiles at four positions, $z/L = 0.5, 0.806, 0.917$ and 0.944. The last position is probably a typographical error in Afgan *et al.* (2006), as position $z/L = 0.944$ in the experimental data (Park & Lee 2000) was only for the case with atmospheric boundary layers at the inlet, and both Afgan *et al.* (2006) and the present work studied only the case with uniform flow at the inlet. The agreement of their C_p with the experimental data is not as good as in the present work, probably as a result of a much coarser resolution than that in the present work. Note that the present fine grid contains approximately 12 times more computational nodes than the fine grid in Afgan *et al.* (2006). According to Afgan *et al.* (2006), the near wall resolution was not fine enough for an accurate reproduction of the development of the
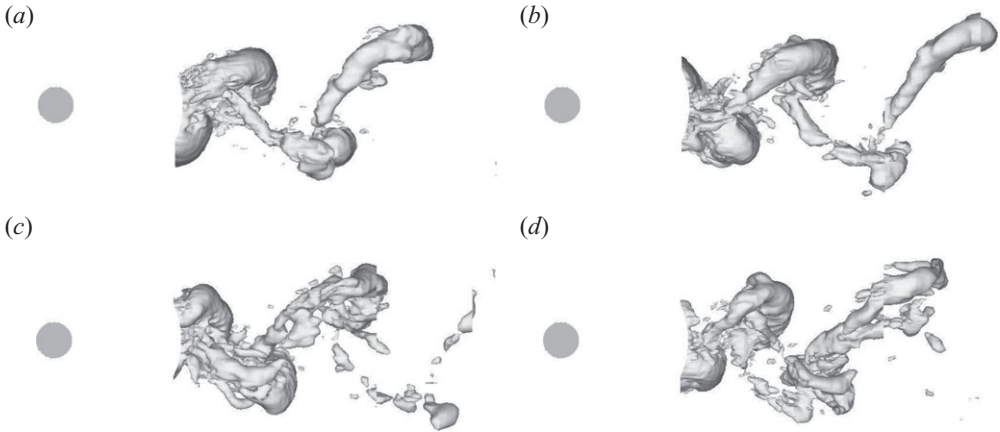
(*a*)   (*b*)

(*c*)   (*d*)

FIGURE 23. Isosurface of static pressure $p = -0.7$. The view is from above. The time
difference between the two pictures is $\Delta t_* = \Delta t U_o / D = 1.2$

boundary layer, and this is probably the reason for the poorer agreement of their C_p results with the experiments. The streamwise velocity component and the streamwise turbulence intensity at position $z/L = 0.5$, $x/D = 5$ were also presented in Afgan *et al.* (2006). These results are very similar to those in the present work. The $\langle \bar{u} \rangle_t / U_\infty$ in Afgan *et al.* (2006) has a minimum at approximately $\langle \bar{u} \rangle_t / U_\infty = 0.5$, similar to that which was found in the present LES and of much lower magnitude than the value measured with hot wire anemometry in Park & Lee (2000). The streamwise turbulence intensity at $z/L = 0.5$, $x/D = 5$ showed a double peak in agreement with the present LES and previous DES by M. Strelets (2005, personal communication) and thus different from the profile with only one peak found in experiments. This shows that all existing numerical simulations predict the recirculation length to be shorter than the one measured in the experiments using hot wire anemometry, which again raises the question of whether the hot wire is an appropriate measuring technique in very turbulent flow in the near wake behind the cylinder. The side force coefficient computed in Afgan *et al.* (2006) showed a non-dimensional frequency of $St = 0.132$, which is close to the experimental value of 0.141 and the present LES value of 0.149. (Note that the experimental value of the frequency was 47 Hz, which gives $St = fD/U_\infty = 0.141$ for $D = 0.03$ m and $U_\infty = 10$ m s^{-1}. The paper by Afgan *et al.* (2006) has a typographical error for this frequency as $St = 0.135$, but the correct value is 0.141.)

7. Conclusions

The flow around a tall finite cylinder was investigated using LES. This flow poses challenges for both experimental and numerical investigations, and the aim of the present paper was to provide a complete flow picture. The LES requires great computational effort to resolve this flow due to complicated flow physics including flow processes such as transition in the shear layer along the cylinder, impingement and formation of horseshoe vortices and bluff body flow around the cylinders free end. However, the LES offers high accuracy in the prediction and the resulting flow (both instantaneous and time-averaged) in the entire domain and for all times (during the simulation) that can be explored in post processing. This advantage of LES was used here to confirm previous knowledge about this flow and fill in the missing gaps.

The flow around the cylinder's free end has been much debated in recent years and its description is still controversial. The previous investigations (Park & Lee 2002, 2004; Pattenden *et al.* 2005) described the formation of the time-averaged tip vortices on the free end. The present work shows that the instantaneous flow contains two pairs of vortices at the position of the time-averaged tip vortices. Each pair consists of two counter-rotating vortices of which the outer vortex (i.e. the one that is further away from the cylinder's symmetry plane) is stronger and has the same direction of rotation as the time-averaged vortex. The assumption of Roh & Park (2003) about the two vortices originating from the focal points on the cylinder's top surface that bend over to form streamwise vortices was questioned before (Pattenden *et al.* 2005; Palau-Salvador *et al.* 2010), and the present investigation provides the final evidence against the flow structures suggested in Roh & Park (2003). Instead, the flow picture of a single vortex (V_{f1} in figure 17) attached to the free end at the two focal points suggested by Pattenden *et al.* (2005) and Kawamura *et al.* (1984) was confirmed.

The near wake flow is another flow region for which we have received better understanding in the present work. Most previous descriptions of this part of the flow are either of short cylinders (Fröhlich & Rodi 2004; Pattenden *et al.* 2007) or of cylinders immersed in thick boundary layers (Sumner *et al.* 2004). Only the recent investigation by Palau-Salvador *et al.* (2010) provides a description of this flow region for a taller cylinder ($L/D = 5$ compared with $L/D = 6$ in the present work) and a thin boundary layer. The present work confirms much of what was shown in Palau-Salvador *et al.* (2010) but also adds new knowledge, particularly about the lower part of the near wake flow. The formation and the spatial extension of the counter-rotating legs (N_{wl} and N_{wr} in figure 17) of structure N_w are presented. It was shown that N_w is a separate flow structure which however interacts with the arch vortex near the closure of the separation region of the near wake. The legs of the arch vortex were found to be inclined to an angle of approximately $31°$ with respect to the cylinder's symmetry axis (for the aspect ratio of $L/D = 6$ of the cylinder studied here). Furthermore, it was shown that this angle is defined by the same angle at which flow structures are transported above the cylinder's free end and down into the near wake during the downwash process.

The time-averaged horseshoe vortex system resulting from the impinging flow at the bottom of the cylinder was found to contain at least three horseshoe vortices (H_1, H_2 and H_3 in figure 9). Vortex B_f, resulting from the balance between the separated flow on the cylinder and the backflow (upstream) of the near wake, was found to compete over the flow space with the horseshoe vortices.

The instantaneous structures that contribute to the time-averaged horseshoe vortices are found to change in time. A complete horseshoe vortex can be distinguished from the instantaneous flow structures sometimes, whereas only pieces of such a vortex are visible at other times. In addition to a change in the shape of the instantaneous horseshoe vortex, its position (or the position of its parts) was found to vary with time.

REFERENCES

AFGAN, I., MOULINEC, C. & LAURENCE, D. 2006 Large eddy simulation of flow over a vertically mounted finite cylinder on a flat plate. In *Conference on Modelling Fluid Flow (CMFF'06)*, *The 13th International Conference on Fluid Flow Technologies*, Budapest, Hungary.

BAKER, C. 1980 The turbulent horseshoe vortex. *J. Wind Engng Ind. Aerodyn.* **6**, 9–23.

DAVIDSON, L. & FARHANIEH, B. 1995 CALC-BFC: A finite-volume code employing collocated variable arrangement and cartesian velocity components for computation of fluid flow and

heat transfer in complex three-dimensional geometries. *Rep.* 95/11, Department of Thermo and Fluid Dynamics, Chalmers University of Technology, Gothenburg.

DRIKAKIS, D., HANH, M., MOSEDALE, A. & THORNBER, B. 2009 Large eddy simulation using high-resolution and high-order methods. *Phil. Trans. R. Soc.* A **367** (1899), 2985–2997.

FRÖHLICH, J. & RODI, W. 2004 LES of the flow around a circular cylinder of finite height. *Intl J. Heat Fluid Flow* **25**, 537–548.

HAHN, M. & DRIKAKIS, D. 2009a Assessment of large-eddy simulation of internal separated flow. *Trans. ASME J. Fluids Engng* **131**, 071201 (1–15).

HAHN, M. & DRIKAKIS, D. 2009b Implicit large-eddy simulation of swept-wing flow using high-resolution methods. *AIAA J.* **47** (3), 618–930.

HAIN, R., KÄHLER, C. J. & MICHAELIS, D. 2008 Tomographic and time resolved PIV measurements on a finite cylinder mounted on a flat plate. *Exp. Fluids* **45**, 715–724.

KAWAMURA, T., HIWADA, M., HIBINO, T., MABUCHI, I. & KUMADA, M. 1984 Flow around a finite circular cylinder on a flat plate (cylinder height greater than turbulent boundary layer thickness). *Bull. JSME* **27** (232), 2142–2159.

KRAJNOVIĆ, S. & DAVIDSON, L. 2002 Large eddy simulation of the flow around a bluff body. *AIAA J.* **40** (5), 927–936.

KRAJNOVIĆ, S. & DAVIDSON, L. 2003 Numerical study of the flow around the bus-shaped body. *Trans. ASME J. Fluids Engng* **125**, 500–509.

KRAJNOVIĆ, S. & DAVIDSON, L. 2005 Flow around a simplified car. Part 1. Large eddy simulation. *Trans. ASME J. Fluids Engng* **127**, 907–918.

LEE, T., LIN, C.-L. & FRIEHE, C. A. 2007 Large-eddy simulation of air flow around a wall-mounted circular cylinder and a tripod tower. *J. Turbul.* **8** (29), 1–28.

LUO, S. C. 1993 Flow past a finite length circular cylinder. In *Third International Offshore and Polar Engineering Conference, Singapore, Vol. III, ISOPE: Golden, CO, USA*, pp. 530–534.

LUO, S. C., GAN, T. L. & CHEW, Y. T. 1996 Uniform flow past one (or two in tandem) finite length circular cylinder(s). *J. Wind Engng Ind. Aerodyn.* **59**, 69–93.

MAJUMDAR, S. & RODI, W. 1989 Three-dimensional computation of flow past cylindrical structures and model cooling towers. *Build. Environ.* **24**, 3–22.

NILSSON, H. & DAVIDSON, L. 1998 CALC-PVM: A parallel SIMPLEC multiblock solver for turbulent flow in complex domains. *Internal Rep.* 98/12, Department of Thermo and Fluid Dynamics, Chalmers University of Technology, Gothenburg.

OKAMOTO, S. & SUNABASHIRI, Y. 1992 Vortex shedding from a circular cylinder of finite length placed on a ground plane. *Trans. ASME J. Fluids Engng* **112**, 512–521.

OKAMOTO, T. & YAGITA, M. 1973 The experimental investigation on the flow past a circular cylinder of finite length placed normal to the plane surface in a uniform stream. *Bull. Japan Soc. Mech. Engng* **16**, 805814.

PALAU-SALVADOR, G., STOESSER, T., FRÖHLICH, J., KAPPLER, M. & RODI, W. 2010 Large eddy simulations and experiments of flow around finite-height cylinders. *Flow Turbul. Combust.* **84**, 239–275.

PARK, C.-W. & LEE, S.-J. 2000 Free end effects on the near wake flow structure behind a finite circular cylinder. *J. Wind Engng Ind. Aerodyn.* **88**, 231–246.

PARK, C.-W. & LEE, S.-J. 2002 Flow structure around a finite circular cylinder embedded in various atmospheric boundary layers. *Fluid Dyn. Res.* **30**, 197–215.

PARK, C.-W. & LEE, S.-J. 2004 Effects of free-end corner shape on flow structure around a finite cylinder. *J. Fluids Struct.* **19**, 141–158.

PATTENDEN, R. J., BRESSLOFF, N. W., TURNOCK, S. R. & ZHANG, X. 2007 Unsteady simulations of the flow around a short surface-mounted cylinder. *Intl J. Numer. Meth. Fluids* **53**, 895–914.

PATTENDEN, R. J., TURNOCK, S. R. & BRESSLOFF, N. W. 2002 An experimental and computational study of three-dimensional unsteady flow features found behind a truncated cylinder. In *Third Joint US-European Fluids Engineering Summer Meeting, Symposium on Issues and Perspectives in Ground Vehicle Flows. 24th Symposium on Naval Hydrodynamics Fukuoka, Japan, 8–13 July*.

PATTENDEN, R. J., TURNOCK, S. R. & ZHANG, X. 2005 Measurements of the flow over a low-aspect-ratio cylinder mounted on a ground plane. *Exp. Fluids* **39**, 10–21.

RHIE, C. & CHOW, W. 1983 Numerical study of the turbulent flow past an airfoil with trailing edge separation. *AIAA J.* **21** (11), 1525–1532.

Roh, S. C. & Park, S. O. 2003 Vortical flow over the free end surface of a finite circular cylinder mounted on a flat plate. *Exp. Fluids* **34**, 63–67.

Smagorinsky, J. 1963 General circulation experiments with the primitive equations. *Mon. Weath. Rev.* **91** (3), 99–165.

Sujudi, D. & Haimes, R. 1995 Identification of swirling flow in 3-D vector fields. *AIAA Paper* 95–1715.

Sumner, D., Heseltine, J. L. & Dansereau, O. J. P. 2004 Wake structure of a finite circular cylinder of small aspect ratio. *Exp. Fluids* **37**, 720–730.

Tanaka, S. & Murata, S. 1999 An investigation of the wake structure and aerodynamic characteristics of a finite circular cylinder. *JSME Intl J.* B *Fluids Thermal Engng* **42**, 178–187.

Zdravkovich, M. M. 1997 *Flow Around Circular Cylinders. Vol 1: Fundamentals*, 1st edn. Oxford Science Publications, ISBN 0-19-856396-5.